nature astronomy

Article

https://doi.org/10.1038/s41550-023-02077-8

Observational evidence for cylindrically oriented zonal flows on Jupiter

Received: 6 February 2023

Accepted: 11 August 2023

Y. Kaspi[1], E. Galanti[1], R. S. Park[2], K. Duer[1], N. Gavriel[1], D. Durante[3], L. Iess[3], M. Parisi[2], D. R. Buccino[2], T. Guillot[4], D. J. Stevenson[5] & S. J. Bolton[6]

The atmospheric dynamics of Jupiter are dominated by strong zonal winds engulfing the planet. Since the first gravity measurements taken by Juno at Jupiter, the low-degree gravity harmonics (J_3–J_{10}) have been used to determine the depth and structure of the zonal winds observed at the cloud level, limiting inferences on the deep flows to the wide latitudinal structure of these harmonics. Here, using constraints on the dynamical contribution to gravity at high latitude, we present the gravity harmonics up to $J_{40.}$ We find an excellent correlation between these measurements and the gravity harmonics resulting from the observed cloud-level winds extending inwards cylindrically to depths of ~10^5 bar (3,000 km). These measurements provide direct evidence that the flows penetrate inwards along the direction of the spin axis, confirming the cylindrical nature of the flow, which has been postulated theoretically since the 1970s. Furthermore, this detailed new gravity spectrum allows us to quantify the contribution of the various jets to the gravity signal, showing the dominance of the strong zonal flows around 20° latitude in both hemispheres.

Jupiter's atmosphere is dominated by strong east–west zonal jet streams, which are strongly tied to the planet's iconic red and white stripes[1,2]. There are six pairs of east–west jets in each hemisphere with peak velocities ranging between −50 and 140 m s^{-1} located between 15° and 65° latitude in both hemispheres (Fig. 1a,c). Equatorwards of these jets there is an eastward flow with velocities of ~100 m s^{-1}, which is super-rotating within 6° of the equator[3], and polewards of ±65° the jets disappear and the dynamics become dominated by vortices all the way to the poles. At both poles, there are powerful cyclones with a diameter of ~4,000 km, surrounded by similar-sized circumpolar cyclones (eight in the north and five in the south[4,5]). This picture has become clearer since the arrival of NASA's Juno mission to Jupiter in 2016[6], and as the mission continues to orbit the planet, with the closest approach moving closer to the north pole every orbit, more information is continuously accumulated. More than 7 years into the mission, the cumulative data are revolutionizing our understanding of the atmospheric dynamics of Jupiter[7,8].

One of the first results that emerged from Juno was the measurement of the north–south asymmetry in Jupiter's gravitational field[9]. This has been attributed to the observed north–south asymmetry in Jupiter's cloud-level winds[10], and matched pre-Juno theoretical estimates for the gravity signature as function of flow depth[11]. The precise measurements obtained by the Juno mission, based on tracking of the Doppler shift of a radio signal as the spacecraft is orbiting the planet, allowed to determine that the observed cloud-level flows extend roughly 3,000 km (10^5 bar) beneath the observed cloud deck of Jupiter[10]. This analysis was based on the odd gravity harmonics (J_3, J_5, J_7 and J_9), and the results matched the low-degree even harmonics J_6, J_8 and J_{10} after the contribution from the internal density structure was subtracted[12,13]. These results were also found to be consistent with constraints coming from secular variations in Jupiter's magnetic field[14–16], and the possibility of a stable layer acting to decay the flow at this depth[17]. In this study, using constraints on the high-degree gravity harmonics at high latitudes, we present the gravity harmonics up

---

[1]Weizmann Institute of Science, Rehovot, Israel. [2]Jet Propulsion Laboratory, California Institute of Technology, Pasadena, CA, USA. [3]Sapienza Universita di Roma, Rome, Italy. [4]Observatoire de la Cote d'Azur, Nice, France. [5]California Institute of Technology, Pasadena, CA, USA. [6]Southwest Research Institute, San Antonio, TX, USA. e-mail: yohai.kaspi@weizmann.ac.il

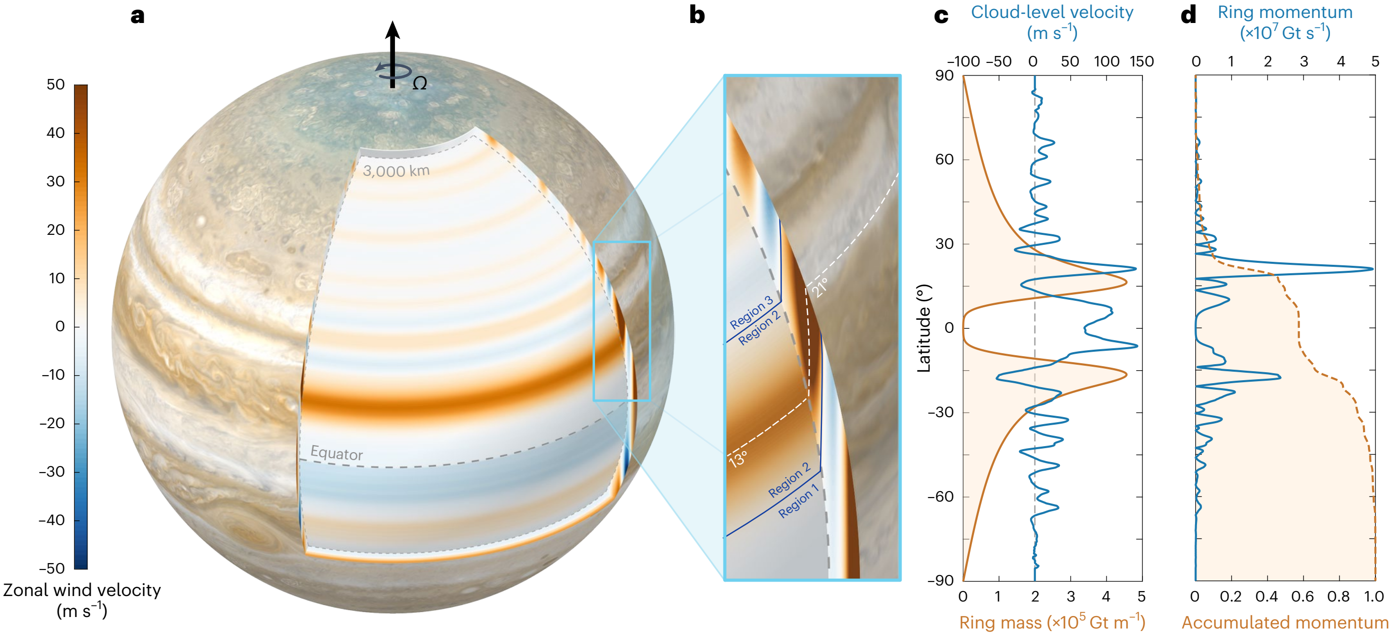

Fig. 1 | Jupiter's zonal flows and their cylindrical orientations. a, 3D illustration of Jupiter's clouds and wind field, where Ω is the planetary rotation rate. The wind field is the zonally averaged zonal wind[58] projected inwards in a direction parallel to the axis of rotation; it decays in the radial direction according to the best-fit solution based on the Juno gravity measurements[10]. The inner shell represents the winds at a depth of 3,000 km. The cloud picture is a combination of Juno and Cassini visible light images. **b**, Close-up of the pale blue rectangle in **a**, showing the cylindrical nature of the strong 21° N cloud-level jet that projects to 13° N at a depth of 3,000 km (Region 2). The white dashed line represents the location of its maximum velocity at all depths. The region closer to the equator (Region 1, outside the tangent cylinder) contains mostly shallow flows, and the region closer to the poles (Region 3) has jets that become weak (<10 m s^{-1}) at 3,000 km depth. **c**, The zonal mean zonal wind at the cloud level[58] (blue), and an estimation of the mass (per metre of a latitude ring) participating in the zonal flows, extending downwards in the cylindrical direction (orange; see 'Calculation of the ring mass' in Methods). **d**, Multiplication of the absolute value of the two curves in **c** (blue), giving an estimate of the wind-induced momentum of each cylindrical ring (per metre in the meridional direction) and the cumulative integral (normalized by the total shell momentum) of the blue curve, starting from the north pole (orange). Credit: image in **a**, NASA/JPL-Caltech/SSI/SWRI/MSSS/ASI/INAF/JIRAM/Björn Jónsson under a Creative Commons licence CC BY 3.0.

to degree 40 (Extended Data Table 1), which we find to correlate well with the calculated wind-induced gravity harmonics. This strengthens the conclusion that the measured gravity anomalies are caused by the winds observed at the cloud level extending inwards. Moreover, the analysis provides direct observational evidence that the cloud-level winds extend inwards along the direction of the spin axis, as has been suggested in theoretical studies[18,19].

The gravity harmonic coefficients (J_n; Methods) are an integrated measure of the planetary density distribution projected on a Legendre polynomial basis function. These have traditionally been used to understand the planetary shape and radial density distribution of nearly spherical objects[7,20,21]. The high-precision gravity measurements taken by the Juno mission[9,22] enabled the detection of small variations in the gravity field due to the flows circulating the planet, which create a geostrophic density anomaly that imprints the gravity signal[10,23]. Thus, the density can be separated into a static component, which is north–south symmetric (as the mean radial density profile has no hemispherical asymmetries), and a dynamical component due to the flows, which has both north–south symmetric and asymmetric contributions[11]. The static component of the gravity harmonics decreases rapidly with increasing degree, while the dynamical component remains roughly the same magnitude for high harmonics due to the latitudinal variability of the wind-induced density variations[24]. This results in the gravity signal beyond J_{10} being fully due to the dynamics (Extended Data Fig. 1). In previous studies gravity measurements could resolve individual harmonics up to J_{10}, meaning that determination of the depth of the flow could be done either by the low-degree odd harmonics (J_3, J_5, J_7 and J_9) or by subtracting the static component of the even harmonics (J_6–J_{10}), based on interior structure models[12] (Extended Data Table 2), from the measurements. Thus, by coincidence, the Juno measurement sensitivity and the degree where the spectrum becomes purely dynamical (for both even and odd) lie at J_{10}. Here we expand the measured gravity spectrum to much higher degrees, allowing us to better resolve the dynamical effects.

Results

Analysis of the high-harmonic gravity signal

The closest approaches of the Juno spacecraft to Jupiter are at low and mid-latitudes, and thus the Juno gravity data sensitivity is saturated near the poles, limiting the number of gravity harmonics that can be resolved. To overcome this limitation, we took advantage of the fact that the zonal flows at high latitudes are weak[25], and that the background interior mass distribution is not expected to contribute to the gravity harmonics beyond J_{10} (ref. 24), and constrained the zonal harmonics beyond J_{12} to less than 1 mGal at high latitudes (Methods). This allowed the gravity harmonics to be resolved up to J_{40} under this assumption. In other words, spatial constraints were applied near the poles so that the recovered high-degree J_n represent the gravity in the latitude band between 40° S and 70° N where the sensitivity of Juno to Jovian gravity is highest. This constraining technique is often used when there is incomplete spatial coverage[26,27].

Under this assumption, the gravity harmonics could be measured to high degree (black data points in Fig. 2a), demonstrating a wavy pattern. This assumption does not affect the low-degree harmonics (J_2–J_{10}) measured without this assumption[28]. The gravity harmonics resulting from the dynamics (red data points in Fig. 2a) were calculated by extending the cloud-level winds inwards along the direction of the spin axis and optimizing their vertical profile so that the wind-induced gravity

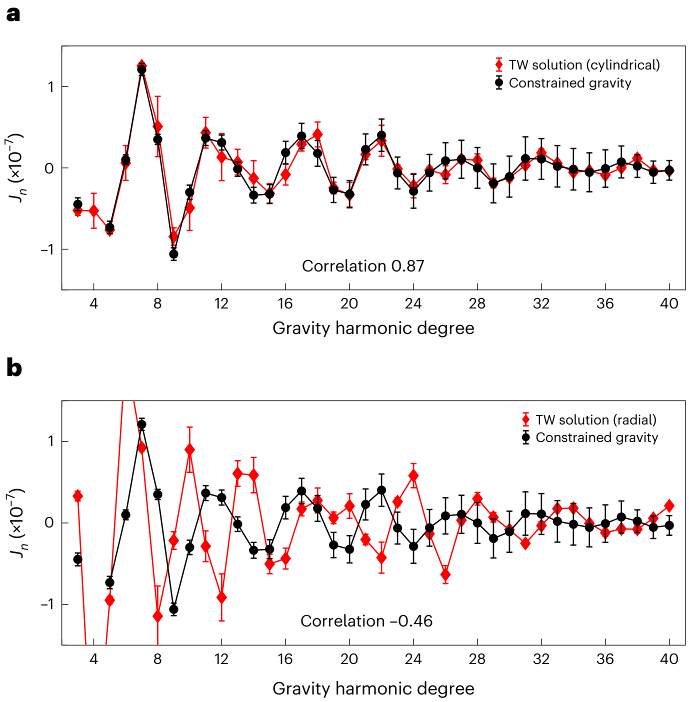

Fig. 2 | Jupiter's gravity harmonics up to J_{40}. **a**,**b**, The measured gravity harmonics with the constrained solution (black) and the corresponding calculated wind-induced gravity harmonics (red) based on projecting the cloud-level winds inwards cylindrically along the direction of the spin axis (**a**) and radially (**b**). In both panels the wind decays with a radial profile $Q(r)$ (Methods, equation (5)), where r is radius. For the measured even harmonics J_6, J_8 and J_{10} we subtracted the non-dynamical values (Extended Data Table 2) coming from internal structure models[12]. J_2 and J_4 were omitted because the relative contribution of the dynamics is very small[12]. The uncertainty in the measurements (black bars) is the 3σ uncertainty (that is, three times the values given in Extended Data Table 1), and for calculated dynamical gravity uncertainty values come the uncertainty in the measured cloud-level winds[58] as shown in the grey envelope in Extended Data Fig. 2.

harmonics matched the measured low-degree odd gravity harmonics (J_3, J_5, J_7 and J_9) as done in previous studies[10,13]. The optimization was performed using the adjoint method[29], and the relation between the wind structure and the density anomalies used to calculate J_n was determined via thermal wind balance[3,23,30] (Methods). Figure 2a shows that the constrained measurements match the dynamical values up to J_{40} remarkably well (correlation of 0.87), indicating that, with very high likelihood, the measured gravity harmonics are due to the winds. It is also evident that this match is associated with the wavy pattern of the signal (explained below), which decreases in power for the higher degrees and has a wavelength of 5–6 harmonic degrees. Note that the gravity harmonics are presented on a linear scale, unlike the traditional presentation of the gravity harmonics on a log scale (Extended Data Fig. 1)[24], which further emphasizes the strong match to the measurements.

The short rotation period of the planet (9.92 h) and the large scale of the dynamics result in geostrophic dynamics[3]. This also implies that theoretically, and if the dynamics are also barotropic, the zonal flow is expected to extend inwards along the direction of the axis of rotation. This has been discussed theoretically since the early papers about Jupiter's dynamics[18,31], demonstrated in laboratory experiments[32] and 3D numerical simulations[19,33–35] and used in numerous theoretical studies[36,37] but never confirmed observationally. The nearly barotropic nature of the flows is known from the fact that they decay inwards very gradually over several thousand kilometres[10] (Extended Data Fig. 2), and thus although not purely barotropic, the decay is weak enough that nearly barotropic dynamics apply[14,38], and the flow is therefore expected to be aligned with the axis of rotation[30]. Here we take advantage of the new knowledge of the high-degree gravity harmonics to show observational evidence for the alignment of the zonal flows with the axis of rotation. Figure 2b shows the same as in Fig. 2a but with the cloud-level winds extended inwards radially, instead of along the spin axis, showing that the high correlation up to J_{40} in Fig. 2a breaks when the flow is not aligned with the spin axis. In both cases presented here the decay of the flow amplitude inwards is radial, assuming that the decay is related to higher pressure, either directly through the denser fluid[3] or due to the magnetic field[14,39]. However, as the specific vertical decay mechanism is unknown, we also explored the possibility that the winds extend inwards cylindrically and that the decay also has a cylindrical orientation (Extended Data Fig. 3). This third option correlates less well with the measurements, but better than the pure radial extension with radial decay. We thus conclude that the best fit is found when the extension is cylindrical but the wind magnitude decays radially.

The source of the wavy gravity signal

Further evidence for the flow orientation can be gained by understanding the origin of the wavy pattern in the gravity signal shown in Fig. 2. To do so, we analysed several simplified profiles of the cloud-level winds (Methods). First, we examined a case in which the winds at all latitudes were set to zero, and only the jet at 21° N was retained (blue line in Fig. 3a). This produced a gravity signal that captured much of the measured signal (Fig. 3b, and see the corresponding density anomaly in Extended Data Fig. 4). To confirm that this jet is setting the frequency of this wavy pattern, we experimented with the wind profile by again keeping only a single jet, but artificially shifting the 21° N jet equatorwards by 5° so that a single jet existed at 16° N (dashed red line in Fig. 3a) and alternately shifting it polewards so that a single jet existed at 26° N (dashed green line in Fig. 3a). The resulting gravity spectra (Fig. 3b) show that none of these synthetic wind profiles matched the data, with the poleward (equatorward) jet shift decreasing (increasing) the wave frequency. This implies that the observed cloud-level winds, and particularly the 21° N jet, set the gravity spectrum. Despite the importance of the 21° N jet, the rest of the winds between 25° S and 25° N did improve the match to observations (black line in Fig. 3c), with most of the secondary contribution coming from the 18° S jet. We further demonstrate this when examining the surface gravity (Fig. 4b).

The dominance of the 21° N jet serves as evidence that the flows extend inwards cylindrically. This can be understood by considering the three regions illustrated in Fig. 1b. In Region 1, outwards of the tangent cylinder (which encompasses a depth of 3,000 km at the equator), there are strong winds at the cloud-level; however, the winds do not penetrate deeply when projected cylindrically, meaning that there is little mass involved in this flow and thus little influence on the gravity harmonics. Therefore the equatorial winds (equatorwards of 17° latitude where the tangent cylinder outcrops the surface), despite being strong, have a negligible contribution to the gravity signal. The integrated cylindrical mass around a latitude circle (Methods), which peaks at 17° latitude, is shown in Fig. 1c. Polewards, in Region 2, where there are the strong jets at 21° N and 18° S, the winds are both strong and penetrate deeply (Fig. 1c) over a region with substantial mass (with a large mass anomaly across the jets; Fig. 1d), and thus contribute strongly to the gravity signal. Previous studies, varying the latitudes of winds[40] or using barotropic winds[41], also demonstrated the importance of Region 2. Note that the jet at 21° N is approximately three times stronger than the jet at 18° S and just slightly less aligned with the region of maximum mass (Fig. 1c), and thus contributes about twice as much to the gravity signal (Fig. 1d). In Region 3, polewards of these strong jets, the jets are weaker and involve less mass (Fig. 1c), and thus their contribution to the gravity signal is small. Note that if the flow projected inwards radially (Fig. 2b), the equatorial flows (Region 1) would have contributed much more to the gravity signal, and the contribution of Region 2 would not

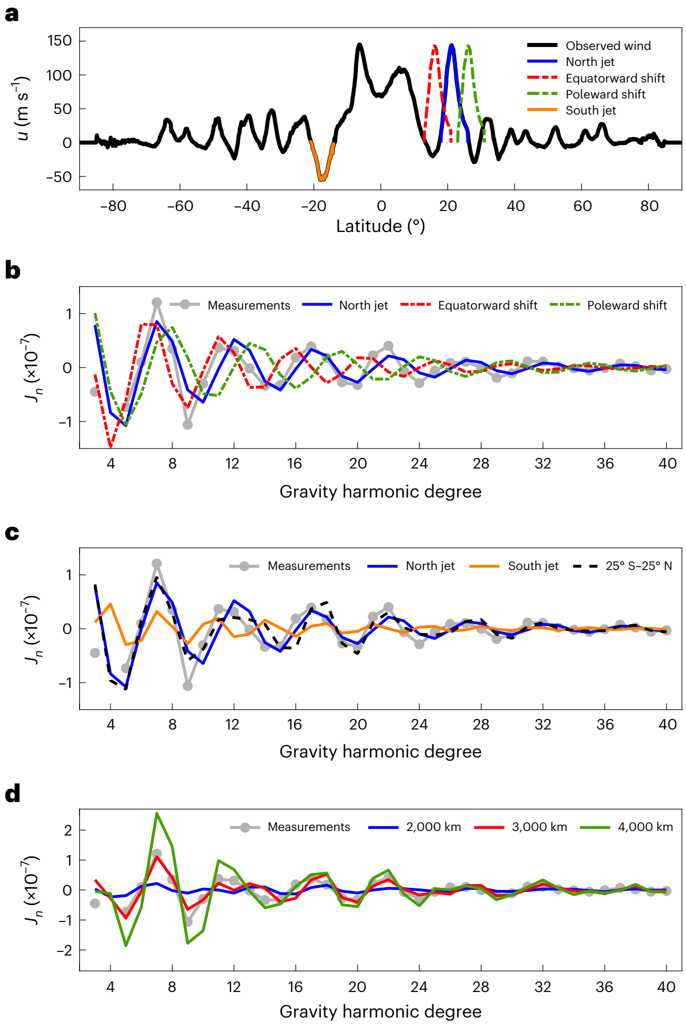

Fig. 3 | The specific jets controlling the structure of the gravity harmonic pattern. **a**, Jupiter's cloud-level winds[58] (black) with the 21° N jet (blue) and the experimental equatorward (red, dashed) and poleward shifts (green, dashed). The 18° S jet is also shown (orange). **b**, Wind-induced gravity harmonics (J_2–J_{40}) resulting just from the 21° N jet and similar jets offset equatorwards and polewards compared with the measurements shown in Fig. 2. The error bars for the measurements are shown in black in Fig. 2 and omitted here for clarity. **c**, The separate contributions of the 21° N jet, the 18° S jet and the full 25° S–25° N region. **d**, The gravity harmonics from the full winds (as in Fig. 2a), considering different decay depths, with the flow decaying to 2% of the surface value at 2,000 km, 3,000 km and 4,000 km (green) (see Extended Data Fig. 2 for radial decay profiles).

have been so dominant. The dominance of the 21° N jet in the gravity harmonics (Fig. 3b) thus serves as direct observational evidence that the flows project inwards cylindrically.

Figure 3b shows clearly that the frequency and decay of the wavy pattern of the gravity signal come mainly from the 21° N jet. The frequency of the wave pattern emerges from the location of the most dominant jet. We illustrate this in Extended Data Figs. 5 and 6 using a simple pulse (Methods) and demonstrate this even analytically in the limit of high harmonics (Methods, where an analytic expression gives the relation between the gravity anomaly location and the wave frequency). The decay of the wave (that is, half of the amplitude at roughly harmonic 20) is set by the width of the jet (gravity pulse), meaning that the narrower the jet is, the longer it takes the signal to decay. The amplitude of this signal comes from the wind penetration depth, as deeper regions are denser and the gravity signal is thus stronger. This is demonstrated in Fig. 3d, which shows the gravity signal resulting from the full winds (black line in Fig. 3a), projected inwards along the direction of the spin axis and decaying radially with a fixed hyperbolic tangent function to different depths (Extended Data Fig. 2). In this analysis, we did not optimize the decay function to allow proper comparison between the solutions. It is evident that the winds decaying to 3,000 km best match the measured gravity harmonics, as shown previously[10]. Interestingly, as the frequency and decay of the wave do not depend on depth, some of the gravity harmonics (which happen to be at the zero crossing of the wave) do not depend on depth. In particular, the wind-induced J_6, which is crucial for interior structure models[42–44], happens to be very close to zero, and thus contributes very little to the overall J_6. This could potentially be used to place stronger constraints on the dynamical J_n used in interior models.

Analysis of the surface gravity at cloud level

Taking a different approach to examining the gravity harmonics, the analysis can be done on the surface gravity itself. Figure 4a shows the surface gravity as function of latitude, taking into account only the first four odd harmonics (the low-order harmonics resulting purely from the dynamics). As expected, there is a match between the measured data from the previous analysis, the new gravity analysis and the calculated wind-induced gravity harmonics. In Fig. 4b we extend the analysis to include all purely dynamical harmonics up to J_N (where $N = 40$, except the early Juno study (blue) where N was 24 and the mid-mission update (green) where N was 30; Methods). The results show that even though the high gravity harmonics of the early analyses[9,28] were very different from the new gravity analysis (Extended Data Fig. 1), their combination is very similar between 40° S and 40° N when mapped to the surface gravity, indicating that the small-scale variability of Jupiter's gravity field was resolved in the previous analyses in this region. The constrained gravity solution (black) matches the full zonal wind-induced profile (red) at high latitudes as well. Setting constraints at high latitudes effectively decorrelates the individual contributions and allows the harmonics beyond J_{10} to be estimated. In the absence of those constraints, the estimation errors for the surface gravity in the polar regions are large as a consequence of the inability to estimate the high-degree harmonics. For this reason, the gravity solutions in the polar regions[9,28], although apparently very different in Fig. 4b, are statistically identical. Note also that in addition to the strong signal due to the 21° N jet, the signal due to the opposing southern hemisphere jet is also evident.

Discussion

This study presents the gravity harmonics of Jupiter to high degree following Juno's multiple flybys of Jupiter, taking into account that the dynamical contribution at high latitudes is small. This new analysis enables resolving several key issues regarding the uniqueness and dynamical balances of the flow field of Jupiter. Deducing the flow field from the gravity spectrum is, by definition, non-unique, as the flow field has endless degrees of freedom and many different flow fields can match a finite number of gravity harmonics. In addition, the gravity is an integrated measure of the mass and thus the non-uniqueness is inherent. The uniqueness question has therefore been hotly debated in the literature[10,45,46], and other flow fields completely unrelated to the cloud-level winds have been suggested[46] and shown to be able to match J_3, J_5, J_7 and J_9. However, the match between the measurements and the gravity signal from the cloud-level winds projected inwards up to J_{40} and the dynamical explanation of the wavy pattern serve as strong evidence that the gravity signal comes from the cloud-level flows. This study also shows that higher-order corrections to thermal wind balance, which have been argued to be necessary for gravity analysis[47,48], can be neglected (Extended Data Fig. 7), as this analysis, using thermal wind balance to relate the flow and the density anomalies[47,49,50], gives a gravity field that correlates very well with the measurements. The same wavy

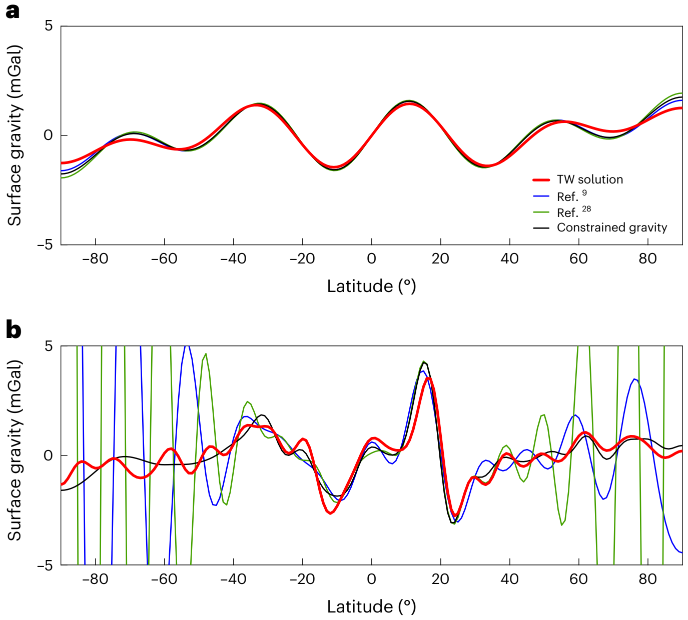

Fig. 4 | The wind-induced surface gravity. a, Jupiter's surface gravity based on the low-degree purely dynamic gravity harmonics (J_3, J_5, J_7 and J_9) using the measurements from the first two gravity orbits (Iess et al.[9]) (blue), the first 10 gravity orbits (Durante et al.[28]) (green), the calculated harmonics based on the cloud-level winds using the thermal wind (TW) balance (red) and the constrained solution presented in this study. **b**, The same as **a**, but using all dynamical harmonics (J_3, J_5, J_7, J_9 and J_{11}–J_N; Methods).

pattern of the gravity signal also explains the signs of the low-degree harmonics J_3, J_5, J_7 and J_9, which were measured early in the Juno mission[9].

Overall, these results confirm that the cloud-level winds imprint the gravity signal, and provide direct evidence of the cylindrical structure of the flows, which penetrate cylindrically down to ~10^5 bar (3,000 km). The cylindrical orientation also implies that the jets are nearly barotropic (via the Taylor–Proudman theorem[30]), particularly in the upper levels, as indicated by the best-matching vertical zonal wind profiles (Extended Data Fig. 2). The 3,000 km depth of the zonal flows, as well as the equivalent 9,000 km depth found on Saturn[14,51], fit well the depth at which electrical conductivity rises on both planets[13], hinting at the connection between the decay of the flow and the magnetic field[39]. Yet, there is no complete mechanism that can quantitatively explain the decay of the flow with depth, and other mechanisms involving compressibility[3] or a stable layer[17,52] have also been suggested. This study provides observational evidence for the structure of the flow at depth, and the next challenge is to mechanistically explain this structure.

Methods

Analysis of the Juno radio Doppler measurements

This study is based on gravity data collected from a total of 26 perijove datasets, where 19 arcs have the two-way dual-frequency (X and Ka band) data[28,53]. The acquisition of the first perijove data started on 27 August 2016 (that is, perijove 1) and the last data considered in this study were taken on 17 October 2021 (that is, perijove 37). To recover Jupiter's gravity field, the external gravitational potential of Jupiter can be modelled using a spherical harmonic expansion:

$$\Phi(r,\theta,\phi) = \frac{GM}{r}\sum_{n=0}^{\infty}\sum_{m=0}^{n}\left(\frac{R_e}{r}\right)^n P_{n,m}\left(\sin\theta\right) \times \left[C_{n,m}\cos\left(m\phi\right)+S_{n,m}\sin\left(m\phi\right)\right], \qquad (1)$$

where G is the universal gravitational constant, M is the mass of Jupiter, R_e is the reference equatorial radius of Jupiter (71,492 km), $P_{n,m}$ are the associated Legendre functions and $C_{n,m}$ and S_{nm} are the unnormalized spherical harmonic coefficients (the corresponding unnormalized zonal harmonics are $J_n = -C_{n,0}$). The gravitational acceleration of an external point source (for example, the Juno spacecraft), defined by the latitude (θ), longitude (ϕ) and radius (r), is given by the gradient of this potential. In this study, the gravity field of Jupiter was modelled with a degree 40 zonal field (that is, J_2–J_{40}) plus four tesseral degree 2 terms (that is, $C_{2,1}$, $S_{2,1}$, $C_{2,2}$ and $S_{2,2}$). For planetary motion, the Jet Propulsion Laboratory's Planetary and Lunar Development Ephemerides 440 (DE440) was used[54]. Other globally estimated parameters were Jupiter's spin-pole motion and tidal Love numbers. For each perijove, locally estimated parameters were the spacecraft state, solar pressure scaled factor and a correction to the first degree 12 zonal coefficients.

Juno's orbit is highly inclined relative to Jupiter's equator (~90–106°) and the periapsis latitude varies from 3.78° to 30.65°. The unconstrained global solution has a sensitivity of up to ~J_{12} as the Juno data sensitivity is saturated near the poles (that is, far from Jupiter when the Juno spacecraft is tracked by NASA's Deep Space Network). A spatial constraint method often used for a sparse dataset was thus applied to extract shorter-wavelength signatures[26,27]. For latitudes between (90° S, 40° S) and (70° N, 90° N), longitude and latitude grids were created for every two degrees, which would be equivalent to having latitude-only constraints scaled by $\sqrt{360^\circ/2^\circ} \approx 13$. For each grid point, the a priori surface acceleration value was constrained to be zero for zonal harmonics J_{13}–J_{40}, with empirically varying a priori determined uncertainties set to reach a mapped a priori surface acceleration uncertainty of 1 mGal. Specifically, for each grid point, the a priori uncertainties were assumed to be 0.04 mGal, 0.1 mGal, 0.2 mGal, 0.3 mGal, 0.4 mGal, 0.1 mGal and 0.04 mGal for latitude bands of (90° S, 80° S), (80° S, 70° S), (70° S, 60° S), (60° S, 50° S), (50° S, 40° S), (70° N, 80° N) and (80° N, 90° N), respectively. With this constraint, the recovered zonal coefficients, J_2–J_{12}, would represent Jupiter's global zonal field, whereas the recovered J_{13}–J_{40} would be a localized solution. In other words, this constraint method extracts the zonal harmonics J_{13}–J_{40} mainly from the latitude band (40° S, 70° N). This constraint technique is similar to the Kaula constraint[26,27,53] but uses a spatial constraint instead of a spectrum constraint. The recovered Jupiter zonal gravity field is shown in Extended Data Table 1. Figure 4 shows that the surface gravity from high-degree harmonics resulting from the estimation of the constrained harmonics J_{13}–J_{40} is about 1 mGal, which is the expected range for gravity anomalies in the polar regions

Given that we were working with a sparse dataset, it was crucial to assess the robustness of the recovered zonal coefficients. One method that is often used for assessing the validity of the estimated values is testing the repeatability of the solution using subsets of data[55]. We tried estimating the zonal harmonics J_2–J_{40} using various subsets of data, such as first half fly-bys, second half fly-bys, every other fly-by and fly-bys with only dual-frequency data. The final reported uncertainties in Extended Data Table 1 were computed by scaling the formal uncertainties of J_{13}–J_{40} by a factor of 1–2 so that the differences between the subset solutions are bounded by the reported uncertainties. Thus, the recovered zonal harmonics and associated uncertainties are statistically valid and robust for the dynamical and measurement models we used in our estimation process. We note that Fig. 2 shows three times these scaled uncertainties (reported in Extended Data Table 1) such that the error bars show a more conservative representation of estimated uncertainties. Even in this conservative case, zonal harmonics up to J_{24} were clearly recovered, and the wavy pattern we explain physically (see 'The source for the waviness in the wind-induced gravity harmonics' below) extends through J_{40}, giving confidence that these high harmonics have a physical meaning even when close to the formal uncertainty.

The vertical wind profile

In this study we examined three different scenarios defining how the wind is expected to be organized below the observed cloud-level wind. In the first scenario, the interior wind was organized into columns reflecting the cloud-level winds:

$$u^{\mathrm{proj}}(r,\theta) = u^{\mathrm{obs}}(\theta'), \tag{2}$$

where $\theta' = \arccos(r\cos\theta/R_e)$ relates the latitude of the interior location θ, to the latitude at cloud level θ', which is at the same distance from the spin axis. Here, u^{obs} denotes the observed cloud-level winds and u^{proj} is their inward projection. This scenario is supported by many studies[18,19,33,34], as discussed in the main text, and was used in the calculation of all results, aside from those shown in Fig. 2b and Extended Data Fig. 3 (see below). In Fig. 2b we examine the second scenario, in which the wind observed at the cloud level was projected inwards in the radial direction, so that:

$$u^{\mathrm{proj}}(r,\theta) = u^{\mathrm{obs}}(\theta). \tag{3}$$

This scenario reflects a hypothetical dynamical situation in which the rotation of the planet does not play a role in the deep structure of the zonal flows.

Given the wind scenario, we then allowed the flow to decay in the radial direction for these two cases, to give the outcoming flow field:

$$u(r,\theta) = u^{\mathrm{proj}}(r,\theta)Q(r), \tag{4}$$

where the radial decay function $Q(r)$ is defined as:

$$Q(r) = (1-\alpha)\exp\left(-\frac{\Delta r}{H}\right) + \alpha\left[\frac{\tanh\left(-\frac{\Delta r - H}{\Delta H}\right)+1}{\tanh\left(\frac{H}{\Delta H}\right)+1}\right], \tag{5}$$

where $\Delta r = R_e - r$, H is the scale height, α is the contribution ratio between an exponential and a normalized hyperbolic tangent function and ΔH is the width of the hyperbolic tangent[10]. This flow field was then used to calculate the gravity perturbation caused by the winds, as discussed below. The choice to make the wind decay radially is based on physical reasoning, as the pressure and density increase radially, resulting in suggested radial decay mechanisms due to compressibility[3], Ohmic dissipation[39] or a stable layer[17]. The values giving the best-fit (to J_3, J_5, J_7 and J_9) of the optimized vertical profile, used in Fig. 2 (Extended Data Fig. 2b, black), were $H = 2{,}101$ km, $\Delta H = 842$ km and $\alpha = 0.68$. For cases where we compared the same profile at different depths (unoptimized to permit a proper comparison in Fig. 3d), the values were $\alpha = 1$, $\Delta H = 500$ km and $H = 1{,}000$ km, $H = 2{,}000$ km and $H = 3{,}000$ km for the blue, red and green profiles, respectively. Note that the quoted values in the legend of Fig. 3d and Extended Data Fig. 2b are for where the flow decays to 2% of the surface flow and not the H value from equation (5). The values for the yellow curve in Extended Data Fig. 2, which includes the magnetic considerations, are $H_M = 200$ km, $f_M = 0.55$ km and $\delta H_T = 204$ km, as discussed in a separate study[14] (see equation (9) in that study). This profile and the best-fitting zonal wind meridional profile[14] give similar gravity harmonics to those shown in Fig. 2a.

A third option we examined was that both the extension of the cloud-level winds and their decays are along the direction of the spin axis (Extended Data Fig. 3). In this case, Δr in equation (5) is replaced by the cylindrical distance $z = R_e\sin\theta' - |r\sin\theta|$. The correlation in this case was lower (0.41) than when the winds extended cylindrically and the decay was radial. In this case, the best optimized case had $H = 3{,}990$ km, $\Delta H = 2{,}057$ km and $\alpha = 0.9$ (Extended Data Fig. 3c). For comparison, Extended Data Fig. 3b has the same H, ΔH and α values as those of the original optimization shown in Extended Data Fig. 3a and Fig. 2a. When the decay is cylindrical the maximum velocity is always at the outer levels of each cylinder (which is not necessarily the case in the radial decay case); this should be taken into account when further investigating the decay mechanism[17,56].

Calculating the wind-induced gravity harmonics and surface gravity

The gravity field, a measure of the planetary mass distribution, depends on the zonal winds via a balance between the anomalous density field and the flow field, as expected in large-scale flow on fast-rotating planets such as Jupiter[23]. Here we give a short version of the derivation of this balance (for the full derivation refer to other studies[10,37,49,50]). The momentum balance, under the assumption of a small Rossby number (large-scale motions on a fast-rotating planet) and a steady state, is:

$$2\Omega \times (\rho\mathbf{u}) = -\nabla p - \rho g - \rho\Omega \times \Omega \times r, \tag{6}$$

where $\mathbf{u}$ is the 3D flow vector, Ω is the planetary rotation rate, ρ is density, p is pressure and g is the gravitational acceleration[30]. Separating the solutions to a rigid body solution $\rho_s(r,\theta)$, $p_s(r,\theta)$ and $g_s(r,\theta)$ in which $\mathbf{u} = 0$, and a deviation due to the dynamics $\rho'(r,\theta)$, $p'(r,\theta)$ and $g'(r,\theta)$, the dynamical balance becomes:

$$2\Omega \times (\rho_s\mathbf{u}) = -\nabla p' - \rho_s g' - \rho' g_s - \rho'\Omega \times \Omega \times r. \tag{7}$$

Next, neglecting all terms including g' and the centrifugal term, which are of lower order[50] (Extended Data Fig. 7), assuming sphericity (with ρ_s, p_s and g_s becoming radial functions only) and taking the curl results in the zonal component of equation (7) becoming:

$$2\Omega r\frac{\partial}{\partial z}(\rho_s u) = g_s\frac{\partial\rho'}{\partial\theta}, \tag{8}$$

where z is the direction of the spin axis. Given a zonal flow field u, this equation can be solved for ρ' up to an integration constant $\rho_0(r)$ that does not affect the gravity harmonics[10,49]. The wind-induced gravity harmonics were calculated as the volume integral of ρ' projected onto Legendre polynomials:

$$\Delta J_n = \frac{2\pi}{MR_e^n}\int_0^{R_e} r^{n+2}\mathrm{d}r \int_{\theta=-\pi/2}^{\pi/2} P_n(\sin\theta)\rho'(r,\theta)\cos\theta\mathrm{d}\theta. \tag{9}$$

The calculated odd gravity harmonics $n = 3, 5, 7, 9$ were then compared with the measured values, and an optimal solution for the flow field was found by varying the parameters H, α and ΔH using the adjoint method of optimization[29]. Note that the $(r/R_e)^n$ factor in equation (9) results in the higher harmonics being smaller, but as this factor for the relevant depths (up to 3,000 km) is close to unity, these variations are not large.

The gravity harmonics can be used to calculate the surface gravity anomaly in the radial direction via:

$$\Delta g_r(\theta) = -\frac{GM}{R_e^2}\sum_n (n+1)\Delta J_n P_n(\sin\theta), \tag{10}$$

with $n = 3, 5, 7, 9$ used in Fig. 4a. In Fig. 4b, in addition to $n = 3, 5, 7, 9$, we also included the high harmonics used in each of the earlier gravity analyses (J_{11}–J_N); that is, harmonics 11–24 for the first 2018 Juno study[9], harmonics 11–30 for updated 2020 Juno study[28] and harmonics 11–40 for the new gravity analysis and the thermal wind solution.

It has been shown that while the term including g' in equation (7) is small, it can still contribute to the low-order gravity harmonics of the order of several tens of per cent[47,48,50]. To estimate this contribution, we adopted the method of Wicht et al.[48] and calculated the gravity harmonics when including the g' term (dynamic self-gravity). The solutions are presented in Extended Data Fig. 7, and are consistent with Wicht et al., confirming that these contributions are small.

The wind-induced density anomalies and gravity signal

To better understand the relation between the wind field and the density anomaly structure (equation (8)), and the relation between the density anomalies and the detected radial gravity signal at the cloud level presented in Fig. 4 (Δg_r, equation (10)), we examined the three fields together with the wind decay rate, ($Q(r)$, equations (4) and (5)) and the static density component (Extended Data Fig. 4). For a clear comparison, and to allow better understanding of the density anomalies, we present the case of the full wind field (Extended Data Fig. 4b) together with a synthetic case with the 21° N jet wind field alone (Extended Data Fig. 4c), as a substantial part of the gravity signal comes directly from it (Fig. 3). The wind field was composed by projecting the cloud-level wind in a direction parallel to the axis of rotation ($u^{\mathrm{proj}}(\theta,r)$, equation (4)) and multiplying it by the best-fit radial decay function ($Q(r)$, Extended Data Fig. 4a), representing the fraction of the cloud-level wind at every depth. Note that as u^{proj} has no decay, its vertical derivative $\left(\frac{\partial}{\partial z}\right)$ is equal to zero. For the examples presented here, the 3,000 km depth level represents the depth at which the wind decays to about 20% of its original velocity, and it is the decay-rate inflection point (Extended Data Fig. 4g).

The dynamical density resulting from a wind field is calculated using thermal wind balance (equation (8)). To determine the absolute dynamical density, the integration constant was set to zero[49], exemplified in a transition from negative to positive anomalies in the meridional direction (Extended Data Fig. 4e,f), which sums to zero at each depth. Note that this choice does not affect the results, as this radial integration constant does not project on J_n, which are only a function of latitude[49].

It is notable that when the wind field was composed of a single jet (Extended Data Fig. 4c), the resulting dynamical density has a single latitudinal jump (Extended Data Fig. 4f), matching the jet location. This helps to clarify the more complicated dynamical density of the full wind (Extended Data Fig. 4e), where each latitudinal shear matches exactly the location of a jet stream (Extended Data Fig. 4b). In the vertical direction, a clear transition appears at a depth of 1,900 km (black dashed lines, Extended Data Fig. 4). This depth is the transition point between two competing factors, the vertical change of the static density (ρ_s) and the vertical change of the wind decay rate. We can simplify the left-hand side of equation (8) by recalling that the derivative along the direction of the spin axis of u^{proj} is zero and open the derivative, such that:

$$2\Omega r\frac{\partial\left(\rho_{\mathrm{s}}u\right)}{\partial z}=2\Omega r u^{\mathrm{proj}}\frac{\partial\left(Q\rho_{\mathrm{s}}\right)}{\partial z}=2\Omega r u^{\mathrm{proj}}\left[Q\frac{\partial\rho_{\mathrm{s}}}{\partial z}+\rho_{\mathrm{s}}\frac{\partial Q}{\partial z}\right]. \qquad (11)$$

At relatively shallow depths, the static density increases by several orders of magnitude (Extended Data Fig. 4d), making its shear $\left(\frac{\partial\bar{\rho}}{\partial z}\right)$ positive and dominant (Extended Data Fig. 4g, orange). However, deeper than 1,900 km, the wind-decay shear $\left(\frac{\partial Q}{\partial z}\right)$, which is negative, becomes dominant (Extended Data Fig. 4g, yellow), flipping the sign of the shear in equation (11) and resulting in a flip of the sign of the dynamical density.

The radial gravity anomaly at the planet's surface that results from the wind-induced dynamical densities is a summation of the different considered gravitational harmonics and their associated Legendre polynomials. As a single jump in the dynamical density field will contribute to all the gravity harmonics (see main text), similar to a pulse that is represented in the spectral domain (Extended Data Fig. 5), the gravitational harmonics resulting from the 21° N jet wind field are summed to give a gravity anomaly that varies with latitude (Extended Data Fig. 4i). This gravity anomaly represents a large fraction of the full wind gravity anomaly (Extended Data Fig. 4h) as it captures its overall magnitude and some latitudinal variations. This relates to Fig. 1, which intuitively shows that the 21° N jet (or Region 2), being strong and comprising a substantial mass due to its location, produces a major part of the gravitational signal detected by the spacecraft.

Calculation of the ring mass

In Fig. 1c, the orange curve represents an estimation for the ring mass (M_C), projected inwards parallel to the axis of rotation under each latitude, that moves like the projected cloud-level wind. To calculate this mass, we defined a coordinate, z, which is the depth coordinate projected downwards from the cloud level in a direction parallel to the axis of rotation. The radial depth can be calculated as:

$$r\left(\theta,z\right)=\sqrt{R_J^2+z^2-2zR_J\sin\theta}, \qquad (12)$$

where R_J (= 69,911 km) is the mean radius of Jupiter. The column height, defined as the distance parallel to the axis of rotation from each point down to the equatorial plane, is $H_{\mathrm{C}}=R_{\mathrm{J}}\sin\theta$. The column mass is defined as:

$$\int_0^{H_{\mathrm{C}}}\rho_{\mathrm{s}}\,\mathrm{d}z, \qquad (13)$$

where $\rho_s(r)$ is the mean density[12]. To only include the mass fraction that participates in the motion of the cloud-level wind, we also considered the wind decay function[10], $Q(r)$, such that the wind-participating cylindrical ring mass is:

$$M_{\mathrm{C}}=2\pi R_{\mathrm{J}}\cos\left(\theta\right)\int_0^{H_{\mathrm{C}}}\rho_{\mathrm{s}}Q\,\mathrm{d}z. \qquad (14)$$

The source for the waviness in the wind-induced gravity harmonics

To give physical intuition to the wavy nature of the gravity harmonics, we perform a synthetic analysis of a pulse in a real space, and decompose it using the discrete Fourier transform (Extended Data Fig. 5). For simplicity, we decompose a one-dimensional signal in spectral space and show that the results are robust and give the right intuition for decomposing the gravity anomaly to gravity harmonics using Legendre polynomials on a sphere (Extended Data Fig. 6). The pulse is defined as a Gaussian centred around location x_0, with an amplitude A and a width W, such that:

$$y\left(x\right)=A\exp\left(-\frac{1}{2}\left(\frac{x-x_0}{W}\right)^2\right). \qquad (15)$$

Hence, the three factors that define the pulse are x_0, A and W. We examine how each of these factors affected the representation of the pulse in the spectral space. It is well known that the spectral representation of a pulse will include a wavy pattern of different frequencies. The pulse height (Extended Data Fig. 5a) intuitively dictates the amplitude of the wave (Extended Data Fig. 5d), which is well represented in a magnitude plot of the 30 lowest frequencies (Extended Data Fig. 5g). A pulse with infinitesimal width is represented in the spectral space by a 'perfect' wave, such that all wavenumbers contribute equally. This is shown for a very narrow pulse width (Extended Data Fig. 5b, blue), where the 'decay' of the frequencies vanished (Extended Data Fig. 5e,h, blue). However, a wide pulse (Extended Data Fig. 5b, orange) requires fewer wavenumbers (Extended Data Fig. 5e,h, orange), moving the cutoff such that the decay of frequencies is faster. Lastly, a pulse located at the middle of the domain (Extended Data Fig. 5c, yellow) results in a very short wavelength (distance between neighbouring peaks) in the spectral space representation (Extended Data Fig. 5f,i, yellow). Pushing the pulse to the north increases the wavelength, creating a 'smoother' wavy pattern.

We perform a second synthetic analysis of a hypothetical localized gravity anomaly (Extended Data Fig. 6). We start with a Gaussian function with a width of 5° (red line), centred around 16° N, which resembles in character the surface gravity resulting from the observed 21° N jet (Extended Data Fig. 6a, grey line). Note that the surface gravity is composed of all the gravity harmonics J_2–J_{40}. The resulting gravity signal (Extended Data Fig. 6b) shows a wavy pattern, similar to that resulting from the observed wind profiles, that depends on the exact shape of the synthetic surface gravity. A narrower surface gravity signal (2° in width; Extended Data Fig. 6a, blue) results in a wavy pattern that has less variation in the amplitude of the harmonics, while a wider surface gravity signal (8° in width; Extended Data Fig. 6a, green) does not change the lower harmonics, but makes the higher harmonics smaller, leading to a stronger decay. In both cases, there is no effect on the frequency of the wave. This is equivalent to the simple case of changing the pulse width in spectral space. Moving the surface gravity signal in latitude (Extended Data Fig. 6, lower panels) affects the frequency, similar to changing the pulse's location in the simple test above. An equatorward shift (5° in latitude; Extended Data Fig. 6b, blue), increases the frequency, while a similar poleward shift results in a decreased frequency (Extended Data Fig. 6b, green). The fact that the wavy pattern is not 'jumping' in sign between gravity harmonics suggests that the pulse responsible for this signal is off-equatorial, as shown in the simple case above of a centred pulse. Moreover, a pulse close to the pole will create a much 'smoother' wave, hence, the jet location is not surprising due to the specific wavelength of the gravity harmonics. It is also evident that shifting the surface gravity signal does not change the amplitude of the wavy patten in the gravity harmonics, for either the lower or higher harmonics. The amplitude analogy is presented in the main text (Fig. 3d), where the different decay depths generate different amplitudes in the surface gravity signal.

We conclude that zonal jet at 21° N has a localized positive expression in the surface gravity (see also Extended Data Fig. 4), and that the signal, when decomposed into the Legendre polynomials, has a wavy expression in the gravity harmonics. This is equivalent to the much simpler case of a pulse decomposed using a Fourier transform. The frequency of the wavy pattern is set by the latitude of the surface gravity (resulting from the location of the jet), the amplitude of the wave is set by the decay structure and hence the amplitude of the surface gravity signal, and how the wavy pattern decays with higher harmonics is set by the width of the surface gravity signal (resulting from the width of the jet).

An analytical expression for the latitude of the wave source

Expanding on the physical intuition of the previous section, here we derive an idealized analytical expression for the latitude of the wave source. Consider an idealized representation of the gravity anomaly resulting from the 21° N jet, shown in Extended Data Fig. 6a–c (and Extended Data Fig. 4i) in the form of a delta function:

$$\delta\left(x-c\right)=\sum_{n=0}^{\infty}a_nP_n\left(x\right), \tag{16}$$

where P_n are Legendre polynomials and $x = \sin\theta$. This is equivalent to equation (10) with a_n being proportional to J_n. Multiplying by $P_k(x)$, with k being the spectral wavenumber, integrating and using orthogonality, leads to:

$$a_k = \left(k+\tfrac{1}{2}\right)P_k\left(c\right). \tag{17}$$

The asymptotic limit of high-n then gives (equation 8.10.7 of ref. 57):

$$P_n\left(\sin\theta\right)\approx\cos\left[n\left(\frac{\pi}{2}-\theta\right)-\frac{\theta}{2}\right]. \tag{18}$$

Thus, if the wave oscillates with a constant period:

$$n\left(\frac{\pi}{2}-\theta\right)=2\pi. \tag{19}$$

Analysis of the oscillation in Extended Data Fig. 6b provides a mean period of $n = 4.8667$ (for accuracy we extended the spectrum to very high harmonics and averaged the period), and using this value in equation (19) gives $\theta = 16.03°$, which is in excellent agreement with Extended Data Fig. 6a. Consistently, the north shift has a period of $n = 5.2222$, giving $\theta = 21.06°$ in equation (19) and the south shift with a period of $n = 4.5625$ gives $\theta = 11.10°$, both agreeing with what we find in Extended Data Fig. 6. This analysis is also consistent with treating the wind velocity as a delta function, with which similar oscillation frequencies and shift differences are found in Fig. 3.

Data availability

All data are available via Harvard Dataverse at https://doi.org/10.7910/DVN/F63FFC.

References

1. Vasavada, A. R. & Showman, A. P. Jovian atmospheric dynamics: an update after Galileo and Cassini. *Rep. Progr. Phys.* **68**, 1935–1996 (2005).
2. Duer, K. et al. Evidence for multiple Ferrel-like cells on Jupiter. *Geophys. Res. Lett.* **48**, e2021GL095651 (2021).
3. Kaspi, Y., Flierl, G. R. & Showman, A. P. The deep wind structure of the giant planets: results from an anelastic general circulation model. *Icarus* **202**, 525–542 (2009).
4. Adriani, A. et al. Clusters of cyclones encircling Jupiter's poles. *Nature* **555**, 216–219 (2018).
5. Gavriel, N. & Kaspi, Y. The number and location of Jupiter's circumpolar cyclones explained by vorticity dynamics. *Nat. Geosci.* **14**, 559–563 (2021).
6. Bolton, S. J. et al. Jupiter's interior and deep atmosphere: the initial pole-to-pole passes with the Juno spacecraft. *Science* **356**, 821–825 (2017).
7. Stevenson, D. J. Jupiter's interior as revealed by Juno. *Ann. Rev. Earth Plan. Sci.* **48**, 465–489 (2020).
8. Bolton, S. J. et al. Microwave observations reveal the deep extent and structure of Jupiter's atmospheric vortices. *Science* **374**, 968–972 (2021).
9. Iess, L. et al. Measurement of Jupiter's asymmetric gravity field. *Nature* **555**, 220–222 (2018).
10. Kaspi, Y. et al. Jupiter's atmospheric jet streams extend thousands of kilometres deep. *Nature* **555**, 223–226 (2018).
11. Kaspi, Y. Inferring the depth of the zonal jets on Jupiter and Saturn from odd gravity harmonics. *Geophys. Res. Lett.* **40**, 676–680 (2013).
12. Guillot, T. et al. A suppression of differential rotation in Jupiter's deep interior. *Nature* **555**, 227–230 (2018).
13. Kaspi, Y. et al. Comparison of the deep atmospheric dynamics of Jupiter and Saturn in light of the Juno and Cassini gravity measurements. *Space Sci. Rev.* **216**, 84 (2020).
14. Galanti, E. & Kaspi, Y. Combined magnetic and gravity measurements probe the deep zonal flows of the gas giants. *Mon. Not. R. Astron. Soc.* **501**, 2352–2362 (2021).
15. Moore, K. M. et al. Time variation of Jupiter's internal magnetic field consistent with zonal wind advection. *Nat. Astron.* **3**, 730–735 (2019).
16. Bloxham, J. et al. Differential rotation in Jupiter's interior revealed by simultaneous inversion for the magnetic field and zonal flux velocity. *J. Geophys. Res. Planets* **127**, e07138 (2022).
17. Christensen, U. R., Wicht, J. & Dietrich, W. Mechanisms for limiting the depth of zonal winds in the gas giant planets. *Astrophys. J.* **890**, 61 (2020).

18. Busse, F. H. A simple model of convection in the Jovian atmosphere. *Icarus* **29**, 255–260 (1976).
19. Christensen, U. R. Zonal flow driven by deep convection in the major planets. *Geophys. Res. Lett.* **28**, 2553–2556 (2001).
20. Guillot, T. Interiors of giant planets inside and outside the solar system. *Science* **286**, 72–77 (1999).
21. Wahl, S. et al. Comparing Jupiter interior structure models to Juno gravity measurements and the role of an expanded core. *Geophys. Res. Lett.* **44**, 4649–4659 (2017).
22. Folkner, W. M. et al. Jupiter gravity field from first two orbits by Juno. *Geophys. Res. Lett.* **44**, 4694–4700 (2017).
23. Kaspi, Y., Hubbard, W. B., Showman, A. P. & Flierl, G. R. Gravitational signature of Jupiter's internal dynamics. *Geophys. Res. Lett.* **37**, L01204 (2010).
24. Hubbard, W. B. Note: gravitational signature of Jupiter's deep zonal flows. *Icarus* **137**, 357–359 (1999).
25. Grassi, D. et al. First estimate of wind fields in the Jupiter polar regions from JIRAM-Juno images. *J. Geophys. Res. Planets* **123**, 1511–1524 (2018).
26. Konopliv, A. S., Park, R. S. & Ermakov, A. I. The mercury gravity field, orientation, love number, and ephemeris from the MESSENGER radiometric tracking data. *Icarus* **335**, 113386 (2020).
27. Park, R. S. et al. Evidence of non-uniform crust of Ceres from Dawn's high-resolution gravity data. *Nat. Astron.* **4**, 748–755 (2020).
28. Durante, D. et al. Jupiter's gravity field halfway through the Juno mission. *Geophys. Res. Lett.* **47**, e2019GL086572 (2020).
29. Galanti, E. & Kaspi, Y. An adjoint based method for the inversion of the Juno and Cassini gravity measurements into wind fields. *Astrophys. J.* **820**, 91 (2016).
30. Pedlosky, J. *Geophysical Fluid Dynamics* (Springer, 1987).
31. Zhang, K. Spiralling columnar convection in rapidly rotating spherical fluid shells. *J. Fluid Mech.* **236**, 535–556 (1992).
32. Busse, F. H. & Carrigan, C. R. Laboratory simulation of thermal convection in rotating planets and stars. *Science* **191**, 81–83 (1976).
33. Heimpel, M., Aurnou, J. & Wicht, J. Simulation of equatorial and high-latitude jets on Jupiter in a deep convection model. *Nature* **438**, 193–196 (2005).
34. Gastine, T. & Wicht, J. Effects of compressibility on driving zonal flow in gas giants. *Icarus* **219**, 428–442 (2012).
35. Heimpel, M., Gastine, T. & Wicht, J. Simulation of deep-seated zonal jets and shallow vortices in gas giant atmospheres. *Nat. Geosci.* **9**, 19–23 (2016).
36. Liu, J. & Schneider, T. Mechanisms of jet formation on the giant planets. *J. Atmos. Sci.* **67**, 3652–3672 (2010).
37. Cao, H. & Stevenson, D. J. Gravity and zonal flows of giant planets: from the Euler equation to the thermal wind equation. *J. Geophys. Res. Planets* **122**, 686–700 (2017).
38. Duer, K., Galanti, E. & Kaspi, Y. The range of Jupiter's flow structures fitting the Juno asymmetric gravity measurements. *J. Geophys. Res. Planets* **125**, e2019JE006 (2020).
39. Liu, J., Goldreich, P. M. & Stevenson, D. J. Constraints on deep-seated zonal winds inside Jupiter and Saturn. *Icarus* **196**, 653–664 (2008).
40. Galanti, E. et al. Constraints on the latitudinal profile of Jupiter's deep jets. *Geophys. Res. Lett.* **48**, e92912 (2021).
41. Kulowski, L., Cao, H., Yadav, R. K. & Bloxham, J. Investigating barotropic zonal flow in Jupiter's deep atmosphere using Juno gravitational data. *J. Geophys. Res. Planets* **126**, e06795 (2021).
42. Debras, F. & Chabrier, G. New models of Jupiter in the context of Juno and Galileo. *Astrophys. J.* **872**, 100 (2019).
43. Militzer, B. et al. Juno spacecraft measurements of Jupiter's gravity imply a dilute core. *Planet. Sci. J.* **3**, 185 (2022).
44. Miguel, Y. et al. Jupiter's inhomogeneous envelope. *Astron. Astrophys.* **662**, A18 (2022).
45. Galanti, E. & Kaspi, Y. Deciphering Jupiters deep flow dynamics using the upcoming Juno gravity measurements and an adjoint based dynamical model. *Icarus* **286**, 46–55 (2017).
46. Kong, D., Zhang, K., Schubert, G. & Anderson, J. D. Origin of Jupiter's cloud-level zonal winds remains a puzzle even after Juno. *Proc. Natl Acad. Sci. USA* **115**, 8499–8504 (2018).
47. Zhang, K., Kong, D. & Schubert, G. Thermal-gravitational wind equation for the wind-induced gravitational signature of giant gaseous planets: mathematical derivation, numerical method and illustrative solutions. *Astrophys. J.* **806**, 270–279 (2015).
48. Wicht, J., Dietrich, W., Wulff, P. & Christensen, U. R. Linking zonal winds and gravity: the relative importance of dynamic self-gravity. *Mon. Not. R. Astron. Soc.* **492**, 3364–3374 (2020).
49. Kaspi, Y., Davighi, J. E., Galanti, E. & Hubbard, W. B. The gravitational signature of internal flows in giant planets: comparing the thermal wind approach with barotropic potential-surface methods. *Icarus* **276**, 170–181 (2016).
50. Galanti, E., Kaspi, Y. & Tziperman, E. A full, self-consistent, treatment of thermal wind balance on fluid planets. *J. Fluid Mech.* **810**, 175–195 (2017).
51. Iess, L. et al. Measurement and implications of Saturn's gravity field and ring mass. *Science* **364**, eaat2965 (2019).
52. Gastine, T. & Wicht, J. Stable stratification promotes multiple zonal jets in a turbulent Jovian dynamo model. *Icarus* **368**, 114514 (2021).
53. Park, R. S. et al. A partially differentiated interior for Ceres deduced from its gravity field and shape. *Nature* **537**, 515–517 (2016).
54. Park, R. S., Folkner, W. M., Williams, J. G. & Boggs, D. H. The JPL planetary and lunar ephemerides DE440 and DE441. *Astron. J.* **161**, 105 (2021).
55. Park, R. S. et al. Precession of Mercury's perihelion from ranging to the MESSENGER spacecraft. *Astron. J.* **153**, 121 (2017).
56. Wicht, J., Gastine, T. & Duarte, L. D. V. Dynamo action in the steeply decaying conductivity region of Jupiter-like dynamo models. *J. Geophys. Res. Planets* **124**, 837–863 (2019).
57. Abramowitz, M. & Stegun, I. A. (eds). *Handbook of Mathematical Functions with Formulas, Graphs, and Mathematical Tables* (United States Department of Commerce, 1964).
58. Tollefson, J. et al. Changes in Jupiter's zonal wind profile preceding and during the Juno mission. *Icarus* **296**, 163–178 (2017).

Acknowledgements

We thank R. Chemke for helpful discussions. Y.K., E.G., K.D. and N.G. acknowledge support from the Israeli Ministry of Science and Technology (grant number 96958) and the Helen Kimmel Center for Planetary Science at the Weizmann Institute. D.D. and L.I. acknowledge support from the Italian Space Agency (grant number 2022-16-HH.0). All authors acknowledge support from the Juno mission.

Author contributions

Y.K. and E.G. designed the study. Y.K. wrote the paper. E.G. developed the gravity inversion model and performed the calculations. R.S.P. designed the constrained approach and carried out the analysis of Juno gravity data with D.R.B., M.P., D.D. and L.I. K.D. and N.G performed the idealized models interpreting the gravity signal, density structure and ring mass. D.J.S. led the working group within the Juno Science Team and provided theoretical support. T.G. provided theoretical support. S.J.B. supervised the planning, execution and definition of the Juno gravity experiment and provided theoretical support. All authors contributed to the discussion and interpretation of the results.

Competing interests

The authors declare no competing interests.

Additional information

Extended data is available for this paper at https://doi.org/10.1038/s41550-023-02077-8.

Correspondence and requests for materials should be addressed to Y. Kaspi.

Peer review information *Nature Astronomy* thanks Peter Read and the other, anonymous, reviewer(s) for their contribution to the peer review of this work.

Reprints and permissions information is available at www.nature.com/reprints.

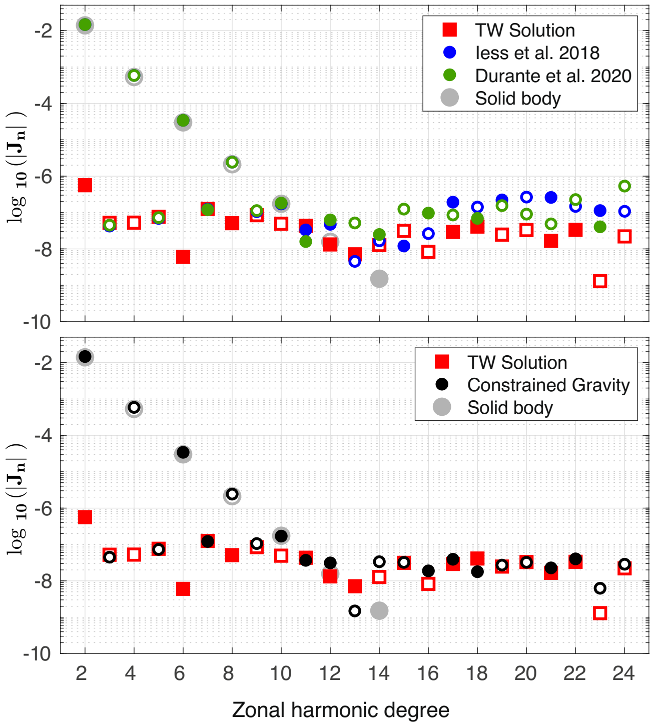

Extended Data Fig. 1 | Jupiter's measured and wind-induced calculated gravity harmonics (J_2-J_{24}) in the standard log-scale. Positive (negative) values are represented in full (open) symbols. Top: the measured gravity harmonics based on the first two gravity orbits (Iess et al.[9]) (blue) and the first 10 gravity orbits (Durante et al.[28]) (green) compared to the calculated gravity harmonics resulting from the cloud-level winds using the thermal wind balance calculation[13] (red), and those arising from solid-body rotation alone[12] (gray). Bottom: The measured gravity harmonics using the constrained solution of this study (black) and the wind-induced gravity harmonics (red).

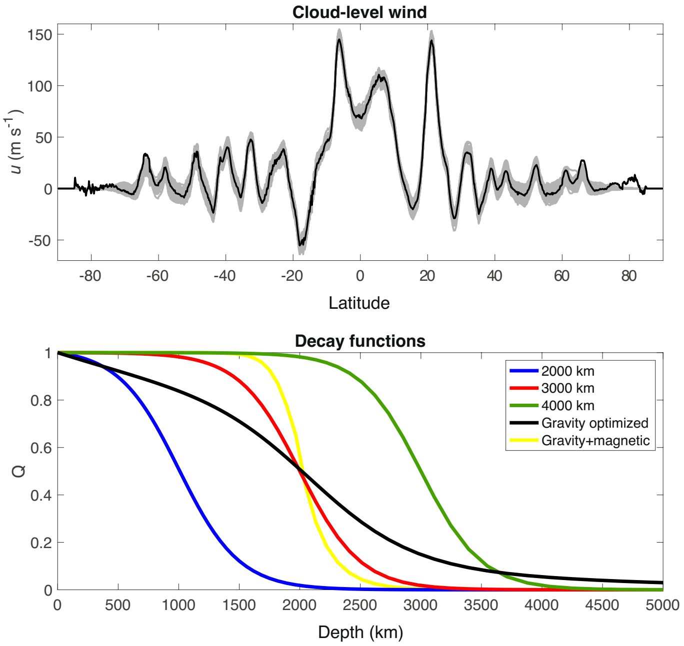

Extended Data Fig. 2 | The meridional and vertical structure of the zonal wind. Top: Jupiter's cloud level winds[58] (black) and their measurement uncertainty (gray) used for the calculation of the error bars in Fig. 2. Bottom: The vertical radial decay function for the cloud-level winds optimized for best matching J_3;J_5,J_7 and J_9 (black)[10], the simplified hyperbolic-tangent functions used for the comparison in Fig. 3d (blue, red and green, corresponding to the colors in Fig. 3d), and the best fitting profile when including magnetic constraints[14] (yellow, in the context of this study it gives similar results to the red profile).

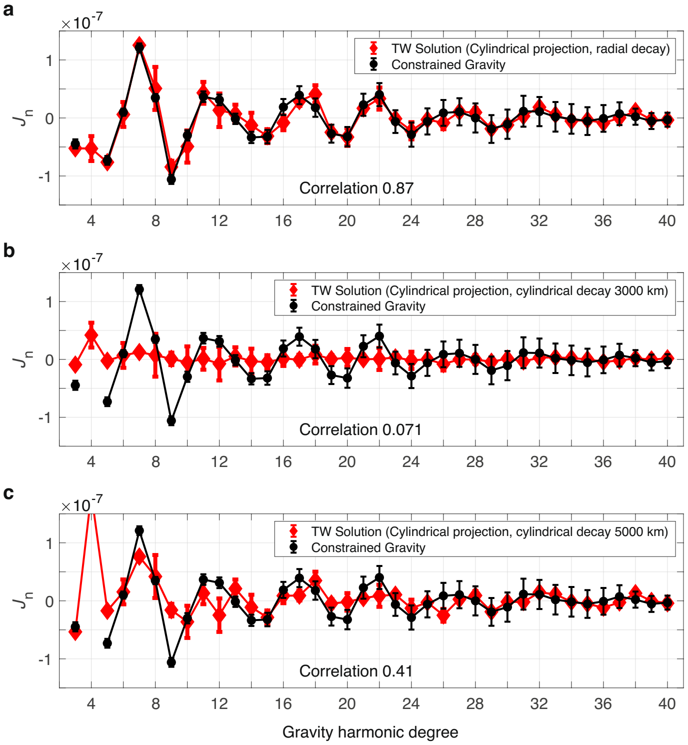

Extended Data Fig. 3 | Experiments with winds decaying in the cylindrical direction. **a.** Jupiter's measured gravity harmonics with the constrained solution (black) and the corresponding calculated wind-induced gravity harmonics based on projecting the cloud-level winds inward (red) cylindrically along the direction of the spin axis (a), as in Fig. 2 in the main text. **b.** A similar analysis, but with the wind decay being along the direction of the spin axis (*z*) instead of radially as done in the rest of the paper (using the same depth as in Fig. 2b). **c.** Same as (b), but with the decay being at 5000 km (the best optimized value).

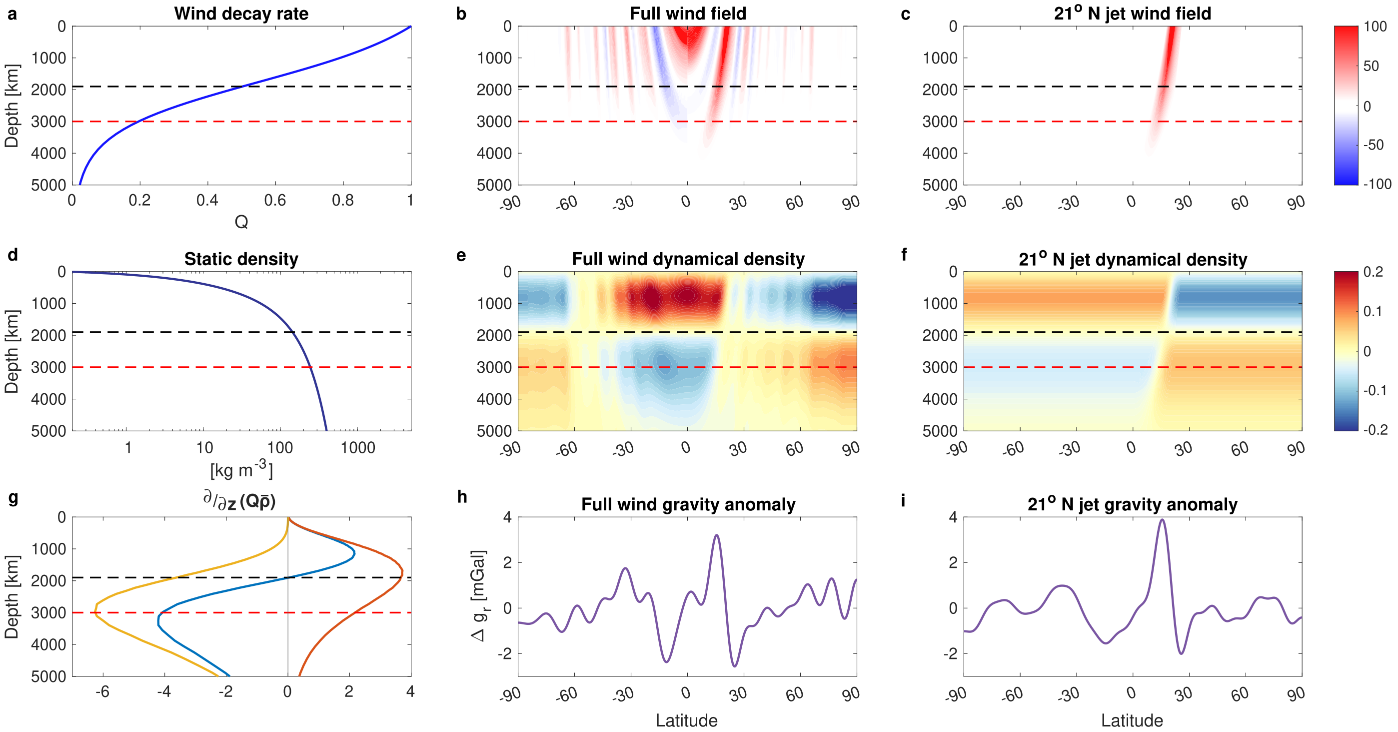

Extended Data Fig. 4 | The density anomaly balancing the wind field. a. The wind decay rate ($Q(r)$) as in Extended Data Fig. 2 (black) used for both examined wind profiles in this figure. **b**. Jupiter's full wind field[58], ms^{-1}, projected inward in a direction parallel to the axis of rotation, and decaying radially according to panel a. **c**. same as panel b, but with only the cloud-level jet of 21° N, ms^{-1}. **d**. The static density component (ρ(r), kg m^{-3}), which varies only with radius. **e**. and **f**. The dynamical density component (ρ', kg m^{-3}) associated with the full wind field (panel b) and the 21° N jet (panel c) according to TW balance (Eq. 8), respectively. **g**. The vertical shear of the multiplication of panels a and d ($\partial/\partial_z(Q\bar{\rho})$, blue), the vertical shear of panel a ($\partial Q/\partial z$, yellow), and the vertical shear of panel d ($\partial\bar{\rho}/\partial z$, orange). **h**. and **i**. The gravitational anomaly, mGal, at the cloud-level, associated with the density field from panel e and f, respectively. The gravity anomaly was reconstructed with J_3, J_5, J_7, J_9 and $J_{11\text{-}40}$; see Eq. (10). In a-g the dashed black line represents a depth of about 1900 km from the cloud-level, where the vertical shear in panel g (blue) changes sign. Dashed red line represents the 3000 km depth, where the vertical shear of panel a ($\partial Q/\partial z$, yellow line in panel g) is minimal, representing the inflection depth.

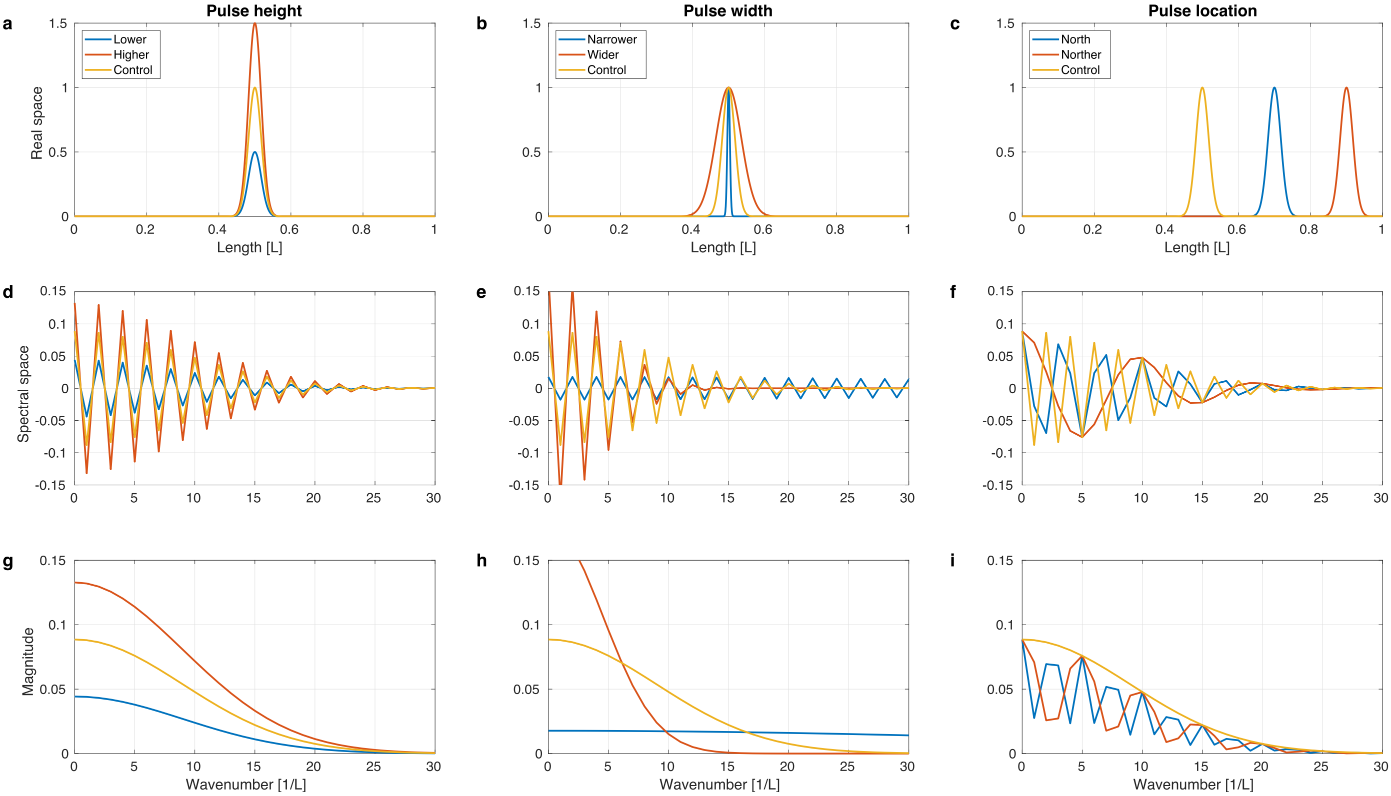

Extended Data Fig. 5 | A synthetic Gaussian pulse represented using Fourier transform. Three tests are performed: different pulse heights (left panels), different pulse widths (middle panels), and different pulse locations (right panels). Each test is shown in the real space **a-c**, in spectral space **d-f**, and in a magnitude plot (absolute value) **g-i**. A control experiment is equivalent in all three cases (yellow). See text in Methods for further details.

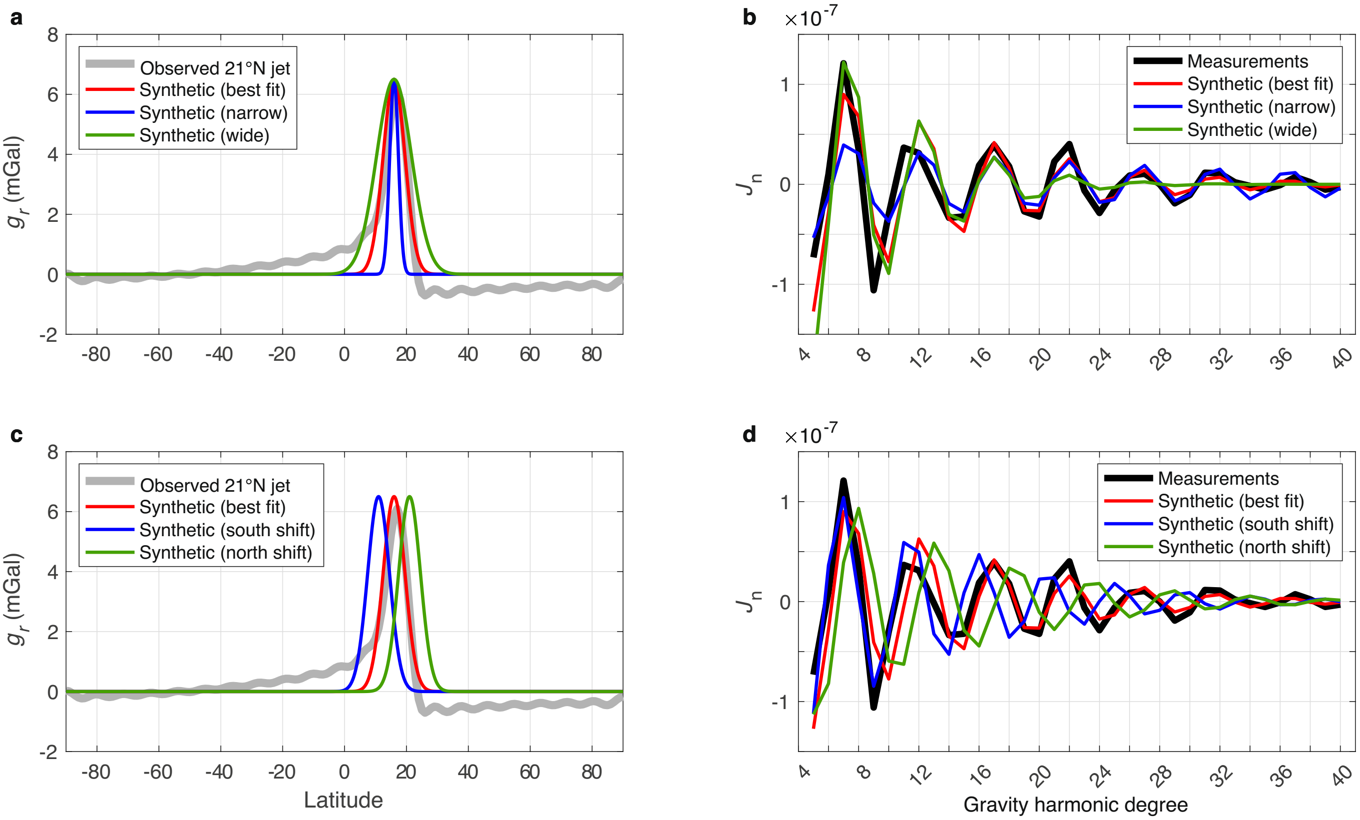

Extended Data Fig. 6 | The surface gravity signal and how it is expressed in the gravity harmonics. a. the surface gravity signal resulting from the 21° N observed jet (gray), and a simple synthetic gaussian function that fits best the observed values (red). Also shown are two variants, a narrower synthetic function (blue), and a wider synthetic function (green). **b**. the measured gravity harmonics (black), and the gravity harmonics calculated from the surface gravity shown in (a). **c**. same as upper panels, but for two other synthetic cases, with the surface gravity shifted poleward (green) and equatorward (blue) by 5°. **d**. the resulting gravity harmonics from (c).

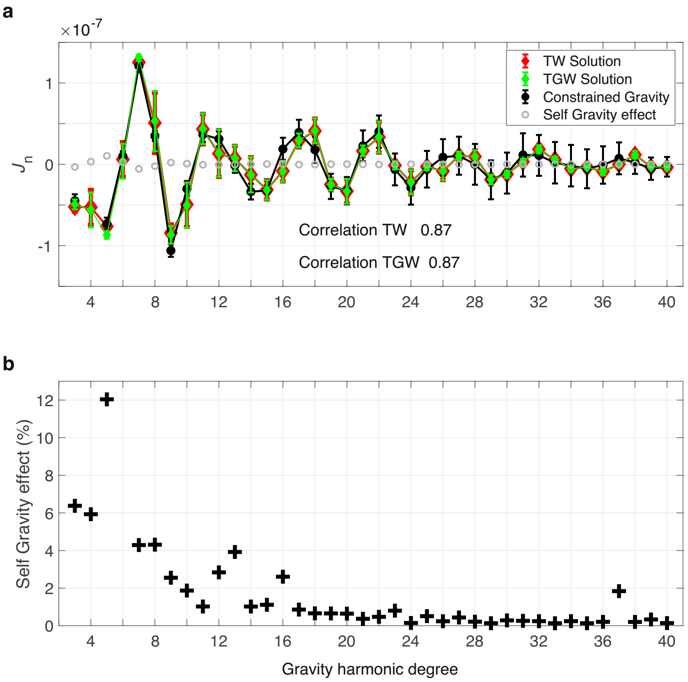

Extended Data Fig. 7 | Comparing the TW and TGW solutions. a. Jupiter's measured gravity harmonics with the constrained solution (black), the corresponding calculated wind-induced gravity harmonics (red) based on projecting the cloud-level winds inward cylindrically along the direction of the spin axis as in Fig. 2 in the main text, and the solution including the self-gravity term as in Eq. (7), using the solution method of Wicht et al., 2020[48] (green). The difference between the two solutions is shown by the gray circles. The results are consistent with those of Wicht et al., 2020. **b**. The relative contribution of the self-gravity term to the gravity harmonics showing the contribution are overall small, particularly for the high-harmonics. The values of J_6 for both the TW and TGW are very close to zero (panel a), and thus the relative contribution is not meaningful and not shown in panel b.

Extended Data Table 1 | Estimated Jupiter zonal harmonics up to J_{40} based on the constraint solution

J_n	Value ($\times 10^6$)	Uncertainty ($\times 10^6$)
J_2	14696.50743	0.00163
J_3	-0.04473	0.00263
J_4	-586.60657	0.00213
J_5	-0.07312	0.00253
J_6	34.19956	0.00203
J_7	0.12102	0.00249
J_8	-2.42483	0.00209
J_9	-0.10600	0.00257
J_{10}	0.16979	0.00295
J_{11}	0.03667	0.00305
J_{12}	0.03118	0.00308
J_{13}	-0.00149	0.00298
J_{14}	-0.03355	0.00324
J_{15}	-0.03220	0.00387
J_{16}	0.01883	0.00461
J_{17}	0.03922	0.00519
J_{18}	0.01784	0.00528
J_{19}	-0.02709	0.00516
J_{20}	-0.03230	0.00557
J_{21}	0.02274	0.00634
J_{22}	0.04023	0.00663
J_{23}	-0.00626	0.00652
J_{24}	-0.02867	0.00695
J_{25}	-0.00598	0.00751
J_{26}	0.00873	0.00742
J_{27}	0.01060	0.00780
J_{28}	0.00000	0.00836
J_{29}	-0.01904	0.00798
J_{30}	-0.01075	0.00840
J_{31}	0.01157	0.00888
J_{32}	0.01099	0.00837
J_{33}	0.00198	0.00850
J_{34}	-0.00163	0.00851
J_{35}	-0.00541	0.00798
J_{36}	-0.00081	0.00767
J_{37}	0.00733	0.00654
J_{38}	0.00217	0.00463
J_{39}	-0.00533	0.00458
J_{40}	-0.00300	0.00401

Jupiter zonal harmonics up to J_{40} based on the constraint solution and using Juno data collected from PJ01 to PJ37.

Extended Data Table 2 | Values for solid-body J_n taken from interior structure models

J_6	34.1880
J_8	−2.4608
J_{10}	0.2021

Values for solid-body J_n taken from interior structure models[12,13].